Boosting deep-sea eruptions with induced fuel-coolant explosions

Authors: T. Dürig[1]*, J.D.L. White[1], A.P. Murch[1,2], B. Zimanowski[3], R. Büttner[3], D. Mele[4], P. Dellino[4], R.J. Carey[5], L.S. Schmidt[6] and N. Spitznagel[3]

Affiliations:

[1]Geology Department, University of Otago, New Zealand.

[2]Geology Department, San Jose State University, California, USA.

[3]Physikalisch Vulkanologisches Labor, Universität Würzburg, Germany.

[4]Dipartimento di Scienze della Terra e Geoambientali, University of Bari, Italy.

[5]School of Natural Sciences, University of Tasmania, Australia.

[6]Department of Geosciences, University of Oslo, Norway

*tobias.durig@otago.ac.nz

Summary:

The great majority of Earth's volcanic eruptions occurs unseen beneath the sea[1–3]. Our understanding of them remains at a primitive level, with few direct observations or even samples from known events[3,4]. This observational shortfall is paralleled by our limited understanding of processes active in this high-pressure realm, built on extrapolation of highly pressure-sensitive subaerial processes into seawater's hugely different rheology and thermal characteristics. Though submarine eruptions are immersed in seawater, no active role for it is generally inferred, because analyses of magma-water explosions identify formation of vapour by boiling at the magma-water contact as a key requirement[5–10], and vaporisation is suppressed at high hydrostatic pressures[11–13]. Here we show that the km-deep submarine eruption of Havre volcano in 2012 involved explosive fragmentation of magma by a pressure-insensitive interaction of water with hot magma, here termed induced fuel-coolant interaction. Laboratory fragmentation experiments show how interactions are initiated, and help reveal diagnostic characteristics of both natural and experimental particles. Induced interactions can occur in all wet environments, from subaerial to the deep sea, and may

operate on different planets, as well as with thermally interacting materials other than magma and water.

Main Text:

The 2012 eruption of Havre volcano, Kermadec arc, New Zealand, produced in a day a ~400 km^2 pumice raft [4,14,15], and on the seafloor an abundance of fine ash [16]. We focus on this ash, which signals expenditure of a large amount of energy to fragment magma[17]. It is not a predicted product of eruptions at this depth[13]. Over 35 km^2 on the volcano the ash shows no thinning trend, so the total volume of erupted ash must substantially exceed the 0.1 km^3 in the mapped area[16]. The ash, erupted from 900-1100 m below sea level (bsl), has abundant blocky or curvi-planar shaped particles <125 μm with low vesicularity and stepped fracture surfaces. Abundant fine to very fine ash suggests explosive fragmentation[6], but particle shapes do not match those produced by expansion of magmatic gases. Instead we find fingerprints of thermohydraulic ash generation, specifically "Induced Fuel Coolant Interaction" (IFCI), and present here experimental evidence for its role at Havre. IFCI aids ash production and increases explosivity during submarine eruptions, and for deep-water volcanic eruptions is likely to be the dominant ash-forming process.

Kindred explosive processes - MFCI and IFCI

In volcanology highly explosive energy release from interaction of magma, generally basaltic, with water ("Molten-Fuel Coolant Interaction" (MFCI)) is known as the driving mechanism for subaerial phreatomagmatic eruptions [18–21]. The key MFCI process is a thermohydraulic feedback cycle under non-equilibrium conditions (Fig. 1), where heat transferred from hot fuel into entrapped expandable coolant causes strong hydraulic pressure to act on the fuel-coolant interface. Brittle fractures penetrate the fuel and expanding liquid coolant pushes into these cracks, driving within fractions of milliseconds their further

propagation, increases in the interface area, acceleration of heat transfer and release of strong shock-waves. The feedback persists until the system is opened and the superheated entrapped coolant is released as expanding vapour, carrying away with high kinetic energy the crack-bounded fragments.

For deep-submarine eruptions it is a deeply embedded concept that magma-water explosivity is unimportant because it is driven by a vapour phase that is suppressed at high pressures[6]. This limitation does not apply to a process which we introduce here as "Induced Fuel Coolant Interaction" (IFCI). IFCI was recently identified during investigation of a crater-forming eruption of viscous high-silica magma[22], where high magma viscosity prevented the mingling of water (coolant) with magma (fuel) necessary for "classic" molten fuel-coolant interaction (MFCI). Instead, IFCI functions through "shortcutting" initation of the thermohydraulic feedback loop that is the underappreciated core of MFCI explosions. It occurs when coolant enters cracks that open in a fuel being fragmented by other processes. IFCI resembles the MFCI process in how heat is thermohydraulically converted in a feedback loop (see Fig. 1) to release fragmentation energy, but IFCI does not require vapour films and occurs under less restrictive initial and boundary conditions. In this study we show that IFCI can convert heat to produce ash in submarine eruptions at any depth.

We investigated IFCI characteristics and explored its relevance for the 2012 Havre eruption, by conducting two series of fragmentation experiments with crushed and remelted Havre rock together with different ash sampling strategies (Methods). In “dry” runs, melt was fragmented by injecting pressurized gas, whereas in “IFCI” runs a layer of water was added prior to gas injection (see Fig. 2). In IFCI runs, fragments were produced by (1) dry gas-driven cracking, and (2) thermohydraulic processes during IFCI (“IFCI particles”). Thermohydraulic IFCI processes advanced downward in our setup, tracing the opening tensional cracks from the top of the melt. IFCI particles were thus much more abundant in the leading part of the ejected

cloud of fragments than in the following ejecta. In both series of runs ejecta was collected from the ground ("DG" and "IG" for dry and IFCI runs, respectively). IFCI products were also captured in a water bowl positioned alongside the open conduit ("IB"), and as deposits inside water droplets ("IW") adhering to the walls and ceiling around the experimental area (see Extended Data Fig. 1). Furthermore, in a novel subseries of IFCI experiments one end of a U-shaped tube was mounted above the crucible with its other end leading to a water bowl. In these "U-tube" runs, the tube automatically detached ~30 ms after particle ejection began, dynamically separating the leading front of fine particles ("IU", Fig. 2).

We compared the shape of the ash-sized experimental products with natural ash retrieved at six locations close to Havre volcano, labelled "Nat1"-"Nat6" (Extended Data Fig. 1).

Boosting magma fragmentation – IFCI vs dry-fragmentation experiments

The effect of IFCI on fragmentation is evident if maximum recoil force F_{max} is normalized relative to maximum pressure P_{max} and plotted over itself (Fig. 3). Dry runs plot below the dashed line; most IFCI runs plot above. For dry runs F_{max} did not exceed ~2.9 kN (for many, <1 kN), whereas IFCI run peak values reached ~5.8 kN (Extended Data Fig. 2a). In dry runs F_{max} correlates with P_{max} because driving pressure is their only energy source for fragmentation. In contrast, most of the IFCI runs reveal the anticipated thermohydraulic "boost", which added significantly more energy (and thus also entropy) into the process of fragmentation, producing also a considerably larger deviation of data points from the diagonal in the upper IFCI field compared to those in the dry regime. The three outlier IFCI runs (IFCI01, IFCI03 and IFCI09), which plot among the dry runs, did not experience significant interaction of magma with coolant, despite having equivalent initial conditions. This suggests that IFCI energy yield is sensitive to subtle dynamic controls at laboratory

(decimeter) scale. We tested different melt masses (thickness of melt plug), and they had no significant influence on explosivity, nor on the likelihood of achieving efficient IFCI runs.

The increase in fragmentation efficiency with IFCI is also reflected in particle grainsizes. Sieve data for particles $\leq$2 mm ("ash") from seven dry runs and five IFCI runs show increased IFCI fragmentation. On average IFCI runs generated 225% the mass of ash particles as did dry runs (Extended Data Fig. 3). Particularly interesting is the increase in fine ash (<125 μm) – this matches the bulk of seafloor ash discovered at Havre, and is not a particle population predicted as significant for submarine volcanism[13]. The proportion of fine ash with IFCI is ~240% of that produced in dry runs (14.1% vs 5.8%, see Fig. 3c).

Identifying IFCI's morphometric fingerprint

Curvi-planar Havre ash grains do not share the morphology of ground-sampled particles from dry runs (DG) or open IFCI runs (IG), and also fail to match the shapes of any other experimental grains (Fig. 4). We infer that ground-sampled particles from IFCI runs are a mixture of dry-formed and thermohydraulically fragmented grains, with population differences in shape that place them in a separate cluster.

U-tube and wall-sampled particles from IFCI runs show, unlike ground-sampled ones, clear similarities with natural ash samples (Nat1 - Nat6), verified by t-tests and e(quivalence)-tests for all 23 shape parameters. SEM imagery and high-resolution micro X-ray tomography show that these grains share surface features such as steps (Fig. 4). IU contain predominantly grains from the leading ejecta front generated by IFCI, and IW samples show no significant differences to IU ones in any tested shape parameter. Twelve parameters are verified as significantly similar according to e-tests (other shape parameters had large variance differences that precluded meaningful e-tests), indicating high similarity. This suggests that

IW samples originated, like IU samples, from the leading ejecta front, and that in our experiments IFCI processes generated particles with a characteristic morphometric "fingerprint". This fingerprint is shared by Havre's curvi-planar natural grains, which are dominant in Havre's seafloor deposits of fine to extremely fine, 3-8 phi, ash[16]. We therefore infer that IFCI played the major role in generating Havre's ash.

Deep-sea conditions favour IFCI at deep-sea volcanoes

The ratio of thermohydraulic to dry-generated grains in open IFCI experiments is measurably lower than in the Havre deposits, in which curvi-planar particles are dominant[16]. IFCI processes at Havre were thus apparently more efficient than in the lab.

The biggest difference between lab conditions vs. Havre ones is Havre's much higher ambient pressure (0.1 vs ~10 MPa). A mechanical consequence of higher confining pressure is stronger driving of water into opening cracks, and this water ingress is necessary to initiate IFCI. Two thermodynamic factors most strongly control the efficiency of IFCI: heat transfer rates from melt to water (controlling energy available for thermohydraulic conversion) and expansion rates of superheated water that acts as a "wedge" inside the crack (controlling how effectively this energy is converted into mechanical work). Measurements of seawater under oceanic temperatures indicate that thermal expansion rates increase with increasing pressure [23], favouring IFCI under the same deep-sea conditions that suppress the vapour formation needed for MFCI.

Laboratory heat-transfer rates are strongly mediated by vapour almost instantaneously generated when water contacts melt (Leidenfrost effect[20,24]). Unlike for MFCI, no stable vapour film is required for IFCI; instead, vapour films inhibit IFCI because they prevent

153 efficient heat transfer from melt to water. Vapour films are broken down by shock waves[20]
154 and in our experiments collapsed the moment pressurized gas hit the melt plug.
155 Under lab conditions 30% of IFCI runs with water flooding did not produce recognizable
156 IFCI fragmentation (see Fig. 3a). In these "failed" IFCI runs the required pre-condition –
157 synchronous crack opening and water invasion (Fig. 1) – was not met, with possible local
158 film boiling also inhibiting interaction. This observation suggests that IFCI requires a critical
159 density of simultaneous cracking with direct water-melt contact.
160 With increasing water depth and pressure, vapour ceases to impede IFCI. Stable film boiling
161 stops above 1 MPa and at 10 MPa (~1 km bsl) meta-stable film boiling becomes
162 impossible[6,25]. Consequently, higher pressure *favours* IFCI in the deep-sea environment.
163 With no vapour film, water directly contacts melt, and heat transfer rates are solely controlled
164 by the heat-transfer coefficient *h*. There is a slight *h* increase for water under seafloor
165 conditions (Fig. 5a; all parameters used for computation: see Extended Data Fig. 4), e.g.,
166 1495 vs 1481 W/m^{2}K (1508 W/m^{2}K for saline water) at 50°C. Although small (1-2%), this
167 difference favours IFCI at depth and may help establish critical IFCI triggering conditions.
168 Far more important, however, is temperature itself; *h* increases with rising temperature to a
169 maximum at 175°C. There, its value is 1927 W/m^{2}K, ~11.5% higher than for surface water at
170 90°C (1729 W/m^{2}K). As temperature increases heat-transfer rates steadily increase,
171 enhancing thermohydraulic heat conversion by providing more energy for the IFCI process.
172 Water at 10 MPa vaporizes at 310.9°C and can exploit the full range of IFCI intensification,
173 whereas under atmospheric pressure (boiling point ~100°C) it would vaporize and expand,
174 shutting down IFCI much earlier.
175 The evolution of Gibbs free energy *G* (Fig. 5b) also indicates significantly increased
176 efficiency in the high-temperature range achievable only under high-pressure conditions. The
177 change in *G* represents the maximum energy available for mechanical work[26], and *G*'s change

178 with temperature indicates increasing efficiency beyond 100°C under seafloor conditions.
179 Thermodynamically, IFCI processes should thus be more efficient under deep submarine
180 conditions than in the lab.
181
182 **"Explosive" ash generation under unexpected conditions**
183 IFCI is an unusual "explosive" process. This thermohydraulic non-equilibrium mechanism
184 generates fine ash at extreme rates by converting heat into intense mechanical work. It is
185 based on an inherently accelerating feedback mechanism fed by increases in both contact
186 surface and heat-transfer rates, leading to rapid and accelerating expansion at microsecond
187 timescales, an "explosive" rate. However, unlike MFCI, at deep seafloor conditions (or
188 similar ones beneath thick glaciers) no dramatic steam expansion would follow the hydraulic
189 stage. Although considerable kinetic energy release can be expected (based on the observed
190 surplus of F_{max} in the IFCI experiments), the friction of surrounding seawater would cause
191 significantly reduced ejection speeds for ash particles compared to a subaerial volcanic
192 setting. Instead, newly generated fine ash particles would be primarily transported by
193 convective movements of the heated ocean water. Their small settling velocities enable
194 widespread dispersion, but explosive expansion has been effectively suppressed.
195
196 A study of Havre pumice concluded that the pumice-raft-generating phase was not driven by
197 magmatic explosions[15], but the observed 70 km-long vapour plume above the eruptive center
198 of Havre[4] is evidence for high rates of heat and energy transfer during one observed stage of
199 the Havre eruption, and the concomitant bluish semi-opaque plume at the ocean surface,
200 offset from the pumice raft[4], indicates that fine particles (ash) were scattering light down-
201 current from the thermal source of the vapour plume. Fine ash was dominantly produced by

IFCI as curvi-planar particles. We infer that IFCI increased ash production and heat-transfer rates at Havre, fueling ash transport to the surface in a strengthened convective plume.

We conclude that IFCI can operate in all deep-sea eruptive settings, and for all magmatic compositions. The primary effects of IFCI at depth are intensified fragmentation and heat transfer, but without necessary vapour-driven particle transport. Eruptions in which it is a major process are far more energetic than classic (subaerial) "effusive" eruptions, resulting in an increased production of fine ash, yet may lack the jets and plumes driven by gas expansion typifying “explosive” ones. Any process cracking a hot fuel into which a coolant can be driven invites IFCI – its fingerprint can be detected through morphometric analysis of the resulting small particles. Beyond submarine volcanoes, IFCI is insensitive to many controls thought to limit explosive magma-water interaction, and it may be expected with hot dry rocks or other hot brittle materials in the deep ocean, as well as with magmatism beneath thick ice on glacier-bearing planets.

References

1. Crisp, J. A. Rates of magma emplacement and volcanic output. J. Volcanol. Geotherm. Res. 20, 177–211 (1984).

2. White, S. M., Crisp, J. A. & Spera, F. J. Long-term volumetric eruption rates and magma budgets. Geochemistry, Geophys. Geosystems 7, (2006).

3. White, J. D. L., Schipper, C. I. & Kano, K. Chapter 31 - Submarine Explosive Eruptions. in The Encyclopedia of Volcanoes (Second Edition) (ed. Sigurdsson, H.) 553–569 (Academic Press, 2015).

4. Carey, R. J. et al. The largest deep ocean silicic volcanic eruption of the past century. Sci. Adv. (2018). doi:10.1126/sciadv.1701121

5. Board, S. J., Hall, R. W. & Hall, R. S. Detonation of fuel coolant explosions. Nature (1975). doi:10.1038/254319a0

6. Wohletz, K. H. Water/Magma Interaction: Physical Considerations for the Deep

Submarine Environment. in Explosive Subaqueous Volcanism (eds. White, J. D. L., Smellie, J. L. & Clague, D. A.) 25–49 (American Geophysical Union, 2003).

7. Wohletz, K. H. Explosive magma-water interactions: Thermodynamics, explosion mechanisms, and field studies. Bull. Volcanol. (1986). doi:10.1007/BF01081754

8. Zimanowski, B., Büttner, R., Lorenz, V. & Häfele, H.-G. Fragmentation of basaltic melt in the course of explosive volcanism. J. Geophys. Res. Solid Earth 102, 803–814 (1997).

9. Berthoud, G. Vapor Explosions. Annu. Rev. Fluid Mech. (2000). doi:10.1146/annurev.fluid.32.1.573

10. Schipper, C. I. et al. Vapour dynamics during magma–water interaction experiments: hydromagmatic origins of submarine volcaniclastic particles (limu o Pele). Geophys. J. Int. 192, 1109–1115 (2013).

11. McBirney, A. R. Factors governing the nature of submarine volcanism. Bull. Volcanol. (1963). doi:10.1007/BF02597304

12. Kokelaar, P. Magma-water interactions in subaqueous and emergent basaltic. Bull. Volcanol. (1986). doi:10.1007/BF01081756

13. Cas, R. A. F. & Simmons, J. M. Why Deep-Water Eruptions Are So Different From Subaerial Eruptions. Front. Earth Sci. 6, (2018).

14. Jutzeler, M. et al. On the fate of pumice rafts formed during the 2012 Havre submarine eruption. Nat. Commun. 5, (2014).

15. Manga, M. et al. The pumice raft-forming 2012 Havre submarine eruption was effusive. Earth Planet. Sci. Lett. 489, 49–58 (2018).

16. Murch, A. P., White, J. D. L. & Carey, R. J. Characteristics and Deposit Stratigraphy of Submarine-Erupted Silicic Ash, Havre Volcano, Kermadec Arc, New Zealand. Front. Earth Sci. 7, 1–21 (2019).

17. Zimanowski, B., Wohletz, K., Dellino, P. & Büttner, R. The volcanic ash problem. J. Volcanol. Geotherm. Res. 122, 1–5 (2003).

18. Büttner, R., Dellino, P., La Volpe, L., Lorenz, V. & Zimanowski, B. Thermohydraulic explosions in phreatomagmatic eruptions as evidenced by the comparison between pyroclasts and products from Molten Fuel Coolant Interaction experiments. J. Geophys. Res. Solid Earth 107, 2277 (2002).

19. Schipper, C. I. & White, J. D. L. Magma-slurry interaction in Surtseyan eruptions. Geology 44, 195–198 (2016).

20. Büttner, R. & Zimanowski, B. Physics of thermohydraulic explosions. Phys. Rev. E 57, 5726–5729 (1998).

21. Zimanowski, B., Büttner, R., Dellino, P., White, J. D. L. & Wohletz, K. H. Magma–Water Interaction and Phreatomagmatic Fragmentation. in The Encyclopedia of Volcanoes 473–484 (Elsevier, 2015).

22. Austin-Erickson, A., Büttner, R., Dellino, P., Ort, M. H. & Zimanowski, B. Phreatomagmatic explosions of rhyolitic magma: Experimental and field evidence. J. Geophys. Res. 113, (2008).

23. Bradshaw, A. & Schleicher, K. E. Direct measurement of thermal expansion of sea water under pressure. Deep Sea Res. Oceanogr. Abstr. 17, 691–706 (1970).

24. Zimanowski, B., Fröhlich, G. & Lorenz, V. Quantitative experiments on phreatomagmatic explosions. J. Volcanol. Geotherm. Res. 48, 341–358 (1991).

25. Zimanowski, B., Büttner, R., Dellino, P., White, J. D. L. & Wohletz, K. H. Magma–Water Interaction and Phreatomagmatic Fragmentation. in The Encyclopedia of Volcanoes 473–484 (Elsevier, 2015).

26. Grunewald, U. et al. MFCI experiments on the influence of NaCl-saturated water on phreatomagmatic explosions. J. Volcanol. Geotherm. Res. 159, 126–137 (2007).

Methods

Fragmentation experiments

For each run crushed rock of mass m_{melt} was inductively heated under non-equilibrium conditions in a 10 cm diameter cylindrical steel crucible (Materials and Methods in Supplement). Standard runs used 250 g of rock; "light" experiments used reduced m_{melt} of 100 g. Within an 80 minute period, the crushed dome rock material was heated up to a temperature of 1573 K then equilibrated for 30 minutes. It was then cooled over a 30-minute period to the experimental temperature of 1423 K. Throughout this process the crucible was covered by a lid, which did not contact the melt and which was removed only seconds before the experiment.

"Dry run" routines matched those for determining material-specific fragmentation and kinetic energy release rates[27,28]. Pressurized argon was injected from below at 8.5 MPa into a cylindrical plug of melt that behaved brittlely when deformed by the expanding injected gas. Like a glass pane hit by a football, the plug deformed until the critical shear stress was

reached, at which point it broke, with elastically stored energy converted into fragmentation and kinetic energy [27,28]. The pressure of the driving gas was measured, and a force sensor under the crucible recorded recoil of the system.

Heating procedure, geometry and sensor setup for "IFCI runs" were the same as for dry runs, but we added a hosepipe leading to the top of the crucible. Two seconds before the gas valve opened, 240 ml of deionized water flooded the crucible, forming a water layer atop the melt. As a consequence, when injected gas initiated fragmentation, water intruded into the opening cracks and initiated IFCI.

To separately sample leading ejecta, mostly from IFCI, we modified some runs with a U-shaped 10 cm-diameter steel tube mounted so that one opening was a few centimetres above the crucible orifice (see Fig. 2). The other end led to a 600 ml bowl of deionized water. In these "U-tube" runs, small particles (plus water and steam) of the leading ejecta front were guided into the water bowl. The tube remained fixed until larger fragments of the following ejecta entered it (~30 ms after fragmentation began), pushing the U-tube upward and removing it from the particle-ejection path (see Fig. 2c-e; Supplementary Video 1). Fragments ejected after U-tube separation followed free ballistic trajectories and were deposited across the whole experimental area ("ground"). U-Tube separation ensured most fragments in the water bowl were from the leading ejecta front.

Particle sampling

Particles generated by the fragmentation experiments were collected after each run, using three different methods:

- Ballistically transported particles deposited on table and floor (DG and IG, for notation see also Extended Data Fig. 1a) were retrieved using a vacuum cleaner with micro-porous paper bags

345 • Particles generated in open IFCI runs, which were deposited in water droplets on the
346 ceiling and walls (IW, see also Extended Data Fig. 1b), were collected using paper tissues,
347 which were subsequently dried.
348 • Particles collected in "U-tube" runs in the water bowl (IU) were retrieved by using
349 paper filters and were subsequently dried.
350 Glassy vesicular Havre ash grains fit three sub-classes: curvi-planar, angular, and fluidal [16].
351 The experimental grains of the 4 phi (<125μm) sieve fraction were compared with ash
352 particles of the same size from six Havre seafloor sites, "Nat1" to "Nat6" (Extended Data
353 Fig. 1c), and exclusively focused on the curvi-planar grains dominant in Havre ash samples.
354
355 **Grain size analysis**
356 All particles collected were sieved at 1phi intervals down to a grain size of 4phi (64-125μm),
357 with the smallest particles accumulating in the pan. One of the characteristics of fuel coolant
358 interaction processes is the increased production of fine ash grains. In order to check if this
359 effect is also measurable for IFCI on Havre material, the two finest fractions, 4phi (125μm-
360 64μm) and smaller than 4phi (<64μm) were binned, and their mass relative to the total
361 amount of "ash", i.e., particles smaller than -1phi (<2mm), was determined as a ratio.
362
363 **Morphometric analysis**
364 For morphometric analysis, a population of 4phi particles was randomly selected and
365 mounted on carbon-coated tape, ensuring that the grains did not touch one another.
366 Backscatter electron scans were produced with a resolution of 2048 x 1536 pixels, using a
367 Zeiss Sigma® VP FEG scanning electron microscope (SEM). The image of each particle
368 was next isolated and binarized, resulting in a black and white image showing its silhouette,
369 i.e the projection of the particle onto an underlying plane. These binarized images were used
370 as input data for the particle shape analyzer software PARTISAN© [29]. This program was

developed to quantify shapes of particle outlines, based on 5 morphometric systems[30–34], and computes 23 dimensionless shape descriptors (of which several are redundantly used in different systems, sometimes with different labels/names).

Each data set was tabulated, then tested pairwise, e.g. A-B, A-C, A-D, B-C, B-D, C-D, by applying a sequence of statistical tests, following a test procedure presented in an earlier study[35] (see also Extended Data Fig. 5). All tests were performed with the software SPSS©, selecting a level of significance α of 5%.

First a Levene test[36] was used to determine whether the variances between compared data sets were homogeneous or not. As a second step, two-tailed pooled variance t-tests[35,36] or separated variance t-tests[37] were used. We identified parameters of indicated significant differences, without corrections[38], and thereby determined types of experiments that reproduced grains with features *most similar* to the natural Havre ash (for sample sizes and results of each test see can be downloaded from the PANGEA depository[39]). This approach minimises the number of type I errors (indications of differences where there are none).

In order to verify, for any two data sets that did not show significant differences from one another in t-tests, a high degree of similarity, we applied equivalence tests ("e-tests"). This method was introduced for image particle analysis with volcanic ash[40] and tests whether the confidence interval C of the tested data set lies within a given range D, specified by the threshold D_{max}. For C, a range of 5% was used. For mathematical details on this method, the reader is referred to the 2012 study by Dürig et al [40]. E-tests are based on the pooled Student's t-function and thus only provide reliable results for data sets with homogeneous variances. E-test results based on data sets with unequal variances have therefore been omitted and are displayed as "(…)", indicating that no statement about possible equivalence can be made (see Extended Data Tables 2-4).

Ranges of D were calibrated to specific shape parameters of Havre ash by applying e-tests pairwise to the natural curvi-planar ash samples, i.e., the samples of Nat1 to Nat6.

In these 15 benchmark tests, the threshold values for D were increased stepwise, starting from 0.01 by a step size of 0.01, until the test indicated a "significant equivalence" in the respective shape parameter. Variances must be homogeneous for this test, so not every e-test yielded results for each of the tested shape factors. For all shape parameters, however, at least one valid threshold value for D was found. Based on the results of these benchmark tests, the largest of the up to 15 D values was used as the shape parameter-specific threshold D_{max} for testing the experimental grains (Extended Data Tables 1). D_{max} can thus be seen as a quantity which specifies the "natural variation" of the respective parameter. We note, that in this approach it is implicitly assumed that these data sets originate from the same particle population, which implies that the curvi-planar ash particles in Nat1 – Nat6 were generated in the same event.

X-ray microtomography (µ-CT)

For each sample suite, the 3D external morphology of about 30 particles of the grain fraction between 125 and 64 µm was determined by X-ray microtomography using a Bruker Skyscan® 1172 high-resolution µ-CT scanner. Particles were cleaned in an ultrasonic bath and mounted on a graphite rod holder using vinyl glue. Particles were scanned with a pixel size of 0.54 µm, an X-ray voltage of 34 kV, an X-ray current of 210 µA, a rotation step of 0.46°, with no filter and a frame averaging over 5 scans. Bruker's software NRecon© was used to reconstruct the µ-CT projection images into two-dimensional cross sections (slices), using a smoothing parameter of 1, a ring artefact correction index of 4 and a beam hardening correction of 36%. The programs CTAn© and CTVox© (both by Bruker) were used for particle image segmentation, and for rendering and displaying the 3D objects.

Model for computing heat transfer coefficients

We next focus exclusively on the "active" water in the cracks which contribute to IFCI by experiencing thermohydraulic expansion. For IFCI, relevant processes take place at high speeds at scales of microseconds[9]. For these short time periods we assume the most important heat transfer mechanism is conduction. For water intruded into a crack the heat transfer coefficient h can be estimated by:

$$h = \frac{k}{\delta}$$

with k being the thermal conductivity of water and δ the thickness of the boundary layer affected by the heat transfer. Assuming high velocities (see below) and turbulent conditions, the latter parameter can be estimated by[41]:

$$\delta \approx 0.37 \cdot x/R^{1/5}$$

where x is the distance downstream from the start of the boundary layer and Re the Reynolds number:

$$R = \rho u L/\mu$$

where ρ denotes the density, μ the dynamic viscosity, u the velocity of the liquid and L the characteristic linear dimension.

Then the heat transfer coefficient can be approximated by:

$$h \approx \frac{k\cdot(\rho u L)^{1/5}}{0.37\cdot x\cdot \mu^{1/5}}$$

For a first order approximation the following assumptions were made: (1) isobaric conditions are assumed; (2) the thermohydraulically expanding water is rapidly pushed into the crack

with u being limited by the speed of sound u_{sound} (in water): (3) both x and L are identical and are set to 5cm.

Values for k, ρ, u_{sound} and μ were computed for water a) under atmospheric pressure conditions (0.1MPa) at 12 different temperatures, ranging from 5° to 90°C b) under "Havre conditions" with 10MPa pressure at 22 different temperatures, ranging from 5° to 310°C. This was done by using the online software CalcSteam[42] and cross-checking the results against the REFPROP data base from NIST[43]. In the same way, the values for Gibbs free energy were computed. In a third data set, densities were also computed for sea water by applying the online software Ocean Water Density Calculator[44] and using a salinity of 35.5 ppt, a pressure of 10 MPa and 22 different temperatures, ranging from 5° to 310°C, as input parameters. This software uses an empirical law[45] for computing the densities.

The same data was also used to set boundary conditions for computing the speed of sound in sea water via the online software Sound Speed Calculator[46], which is based on an empirical relationship [47]. Importantly, both empirical laws are based (and have only been validated) for oceanic temperatures ranging from 0° to 40°C. For this reason, the display of extrapolated results for sea water was limited to a maximum of 80°C.

Method references:

27. Büttner, R., Dellino, P., Raue, H., Sonder, I. & Zimanowski, B. Stress-induced brittle fragmentation of magmatic melts: Theory and experiments. J. Geophys. Res. Solid Earth 111, 1–10 (2006).

28. Dürig, T. et al. A new method for the determination of the specific kinetic energy (SKE) released to pyroclastic particles at magmatic fragmentation: theory and first experimental results. Bull. Volcanol. 74, 895–902 (2012).

29. Dürig, T. et al. PARTIcle Shape ANalyzer PARTISAN – an open source tool for multi-standard two-dimensional particle morphometry analysis. Ann. Geophys. 61, (2018).

30. Dellino, P. & La Volpe, L. Image processing analysis in reconstructing fragmentation and transportation mechanisms of pyroclastic deposits. The case of Monte Pilato-Rocche

Rosse eruptions, Lipari (Aeolian islands, Italy). J. Volcanol. Geotherm. Res. 71, 13–29 (1996).

31. Cioni, R. et al. Insights into the dynamics and evolution of the 2010 Eyjafjallajökull summit eruption (Iceland) provided by volcanic ash textures. Earth Planet. Sci. Lett. 394, 111–123 (2014).

32. Leibrandt, S. & Le Pennec, J.-L. Towards fast and routine analyses of volcanic ash morphometry for eruption surveillance applications. J. Volcanol. Geotherm. Res. 297, 11–27 (2015).

33. Liu, E. J., Cashman, K. V & Rust, A. C. Optimising shape analysis to quantify volcanic ash morphology. GeoResJ 8, 14–30 (2015).

34. Schmith, J., Höskuldsson, Á. & Holm, P. M. Grain shape of basaltic ash populations: implications for fragmentation. Bull. Volcanol. 79, (2017).

35. Dürig, T., Mele, D., Dellino, P. & Zimanowski, B. Comparative analyses of glass fragments from brittle fracture experiments and volcanic ash particles. Bull. Volcanol. 74, 691–704 (2012).

36. Brosius, F. SPSS 8 Professionelle Statistik unter Windows. (mitp-Verlag, 1998).

37. Welch, B. L. The Generalization of `Student's' Problem when Several Different Population Variances are Involved. Biometrika 34, 28 (1947).

38. Perneger, T. V. What's wrong with Bonferroni adjustments. BMJ 316, 1236–1238 (1998).

39. Dürig, T. et al. Fragmentation experiments with Havre melt: dry and induced fuel-coolant interaction runs. PANGEA https://doi.org/10.1594/PANGAEA.908865 (2019).

40. Dürig, T., Mele, D., Dellino, P. & Zimanowski, B. Comparative analyses of glass fragments from brittle fracture experiments and volcanic ash particles. Bull. Volcanol. 74, 691–704 (2012).

41. Schlichting, H. Boundary Layer Theory. (McGraw-Hill, 1979).

42. Wischnewski, B. CalcSteam. Available at: https://www.peacesoftware.de/einigewerte/wasser_dampf_e.html. (Accessed: 29th August 2019)

43. REFPROP. Available at: https://www.nist.gov/programs-projects/reference-fluid-thermodynamic-and-transport-properties-database-refprop. (Accessed: 29th August 2019)

44. Schlitzer, R. Ocean Water Density Calculator. Available at: http://www.csgnetwork.com/water_density_calculator.html. (Accessed: 29th August 2019)

45. Millero, F., Chen, C., Bradshaw, A. & Schleicher, K. A new high pressure equation of state for seawater. Deep Sea Res. Part A 27, 255–264 (1980).

46. Tomczak, M. Sound Speed Calculator. Available at: https://www.mt-oceanography.info/Utilities/soundspeed.html. (Accessed: 29th August 2019)

47. Fofonoff, P. & Millard Jr, R. C. Algorithms for computation of fundamental properties of seawater. Unesco Tech. Pap. Mar. Sci. 44, 53 (1983).

Acknowledgements:

Lisa Schmid and Dylan Longridge are acknowledged for assisting with particle analysis. We thank Ian Schipper for proof-reading an earlier manuscript. This study was supported by MARSDEN grant U001616; Havre samples were obtained with NSF funding EAR1447559.

Author contributions:

J.D.L.W. designed and supervised the Marsden research project. T.D., J.D.L.W., B.Z., R.B., and A.P.M. conducted the lab experiments at Physikalisch Vulkanologisches Labor, University of Würzburg. T.D. and N.S. sampled the experimental particles. T.D. performed grain size analysis, particle preparation and SEM imaging. T.D. conducted 2D morphometry and statistical analysis of both experimental and natural ash with support from D.M. and P.D.. D.M., P.D. and T.D. conducted X-ray microtomography and image reconstruction. T.D. and L.S.S. computed IFCI-relevant thermal water properties. R.J.C was leader of the NSF cruise and helped formulate the Marsden project. J.D.L.W., R.J.C. and A.P.M. took part at the NSF cruise and collected the dome rock used as starting material for melt fragmentation experiments. R.J.C. and A.P.M. provided Havre ash samples and related meta data, including the bathymetric map. Figures and plots were produced by T.D. and L.S.S.. T.D. and J.D.L.W. wrote the manuscript, with contributions from all the authors.

Competing interests

The authors declare no competing interests.

Additional information

Raw data and results of t-tests, including p-values, t-values and degrees of freedom, are available on the open access data archive PANGEA under the following weblink: https://doi.org/10.1594/PANGAEA.908865 [Note for reviewers: DOI will be activated when paper is accepted. At the moment the link https://doi.pangaea.de/10.1594/PANGAEA.908865 can be used to access the data.]

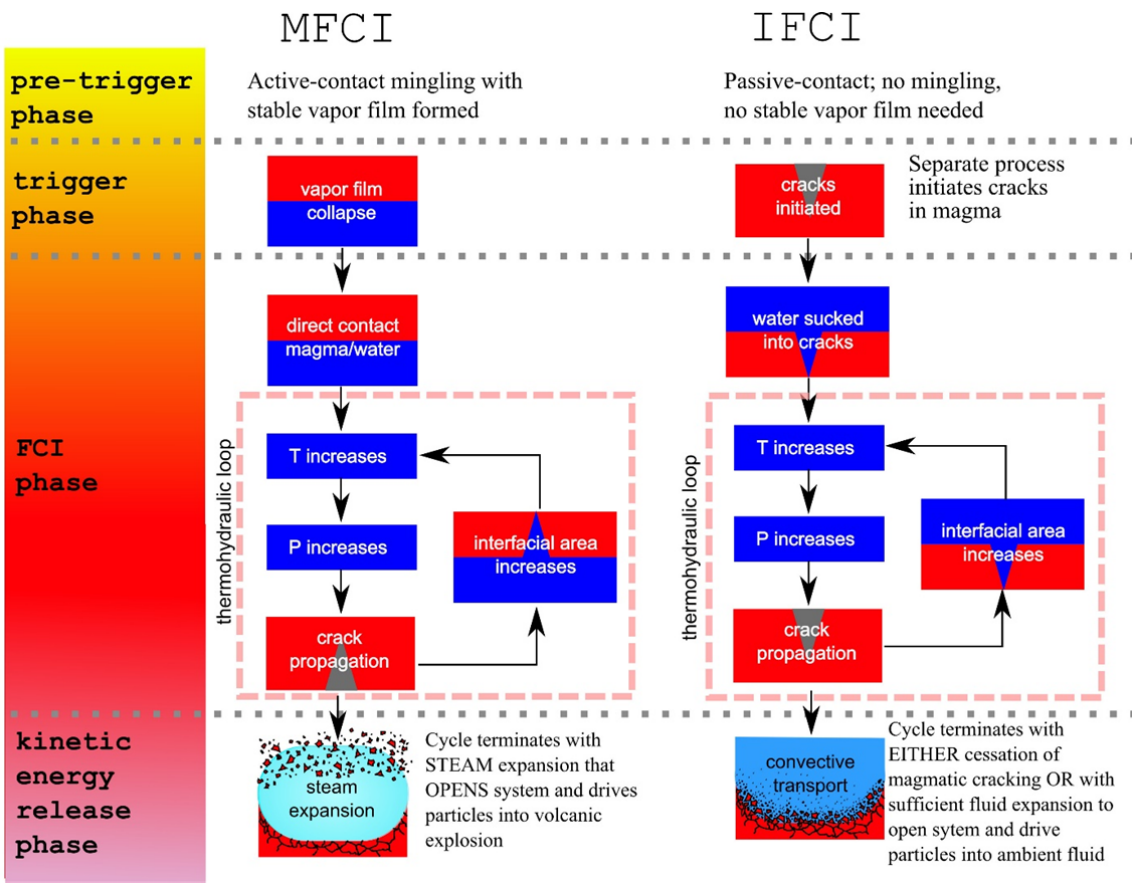

Figure 1| Comparison of molten (MFCI) with induced fuel-coolant interaction (IFCI). Magma (red) is volcanic fuel, and water (blue) the coolant. MFCI needs a pre-trigger vapor film, limiting it to shallow water depths. IFCI initiation requires a sudden increase of the fuel's surface by cracking, *e.g.* by brittle failure of magma highly strained during eruption.

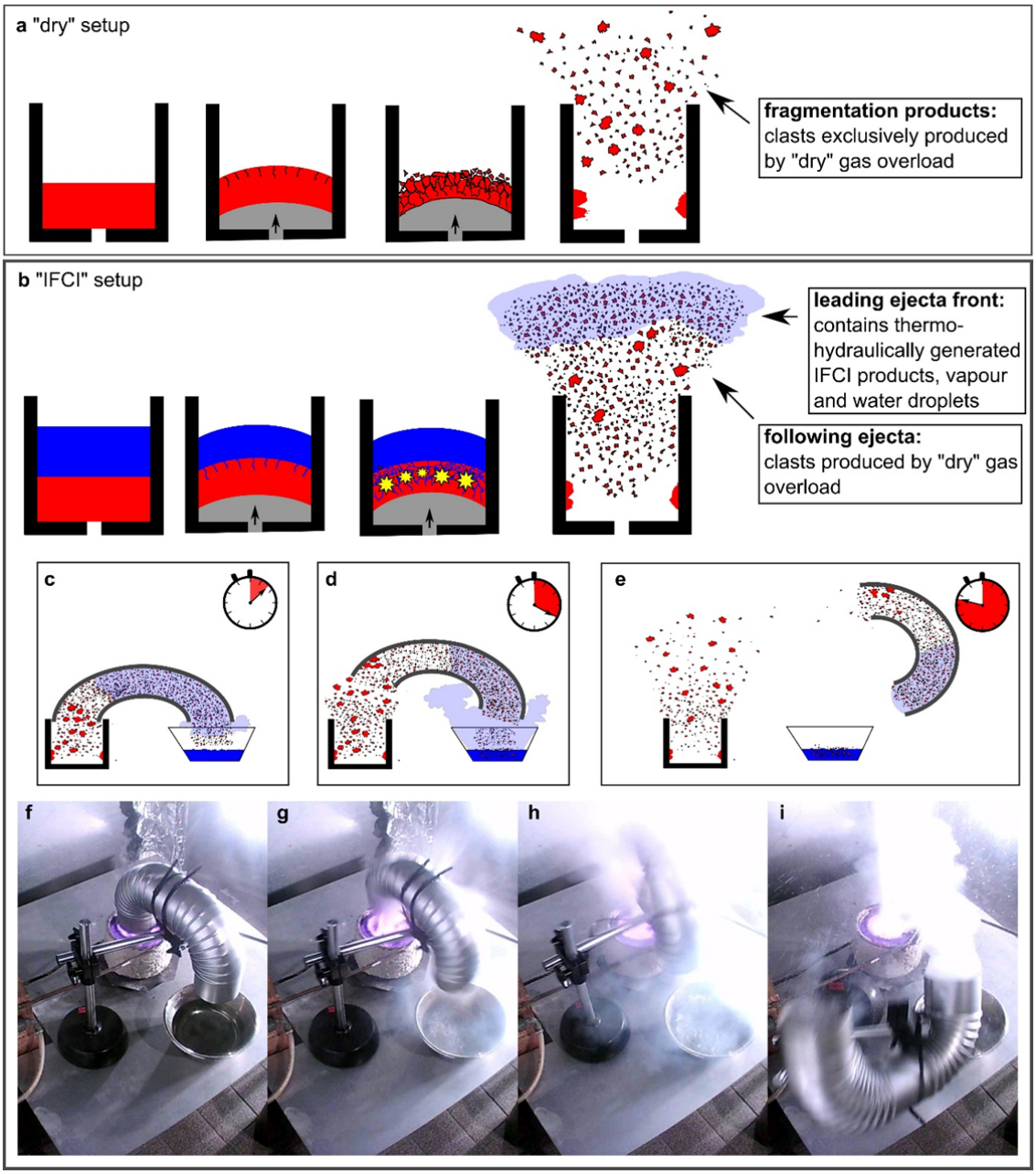

565

566 **Figure 2| Melt fragmentation experiments. a,** For dry runs, the melt plug (red) was deformed by
567 injection of a fixed volume of argon gas, causing stress-induced brittle fragmentation. **b,** for IFCI
568 runs, seconds before gas injection, a water layer above the plug was added, allowing water to intrude
569 cracks opened as gas deformed the plug. This initiated downward-advancing IFCI that
570 thermohydraulically "boosted" fragmentation. With this setup IFCI particles are expected to be most
571 abundant in the leading ejecta front. **c,** in "U-tube" experiments, the fine particles from the leading
572 ejecta front were collected in a water bowl via a U-shaped tube. **d,** the following coarser ejecta
573 particles enter the tube shortly after. Impact momentum causes the tube to detach and **e,** be carried
574 away from the crucible, with very few particles being deposited into the bowl. Bottom-row images are
575 **f,** before the run, and at **g,** 33 ms, **h,** 67 ms and **i,** 167 ms after initiation of fragmentation. The
576 corresponding movie is provided with Supplementary Video 1.

577

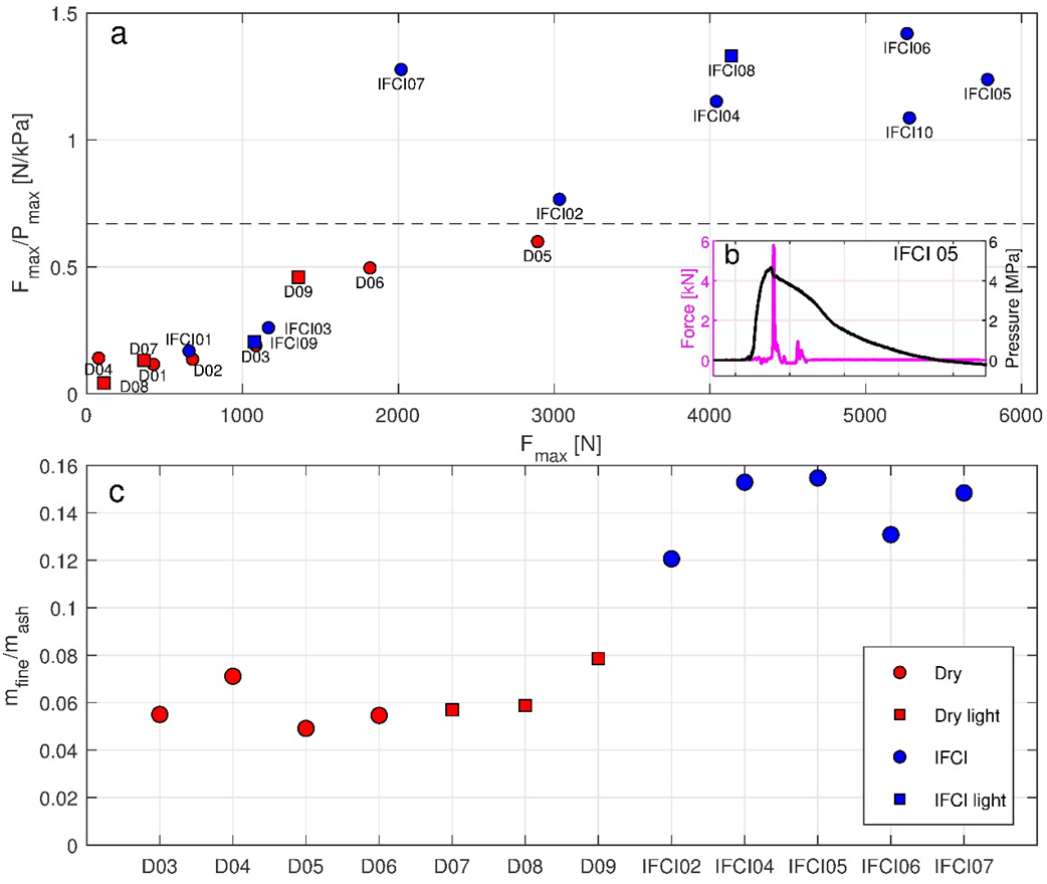

Figure 3| Increased explosivity as measured for IFCI fragmentation experiments. a, for dry (red) and IFCI runs (blue), recoil-force peaks F_{max} were normalized over the maximum driving pressure P_{max} and plotted over themselves. Squares indicate experiments with reduced (100 g) melt mass m_{melt}. Dashed line indicates the empirical boundary between two regimes. Dry runs, with fragmentation driven only by injected gas, plot below the line, whereas most IFCI runs plot above it, reflecting the additional thermohydraulic fragmentation "boost". IFCI runs of low efficiency plot together with dry runs. **b,** example showing pressure (black) and force (magenta) signals for IFCI run plotted over time (range: 250 ms). **c,** the mass ratio of fine ash (<125 μm) over total ash mass is twice as high for IFCI runs than for dry runs.

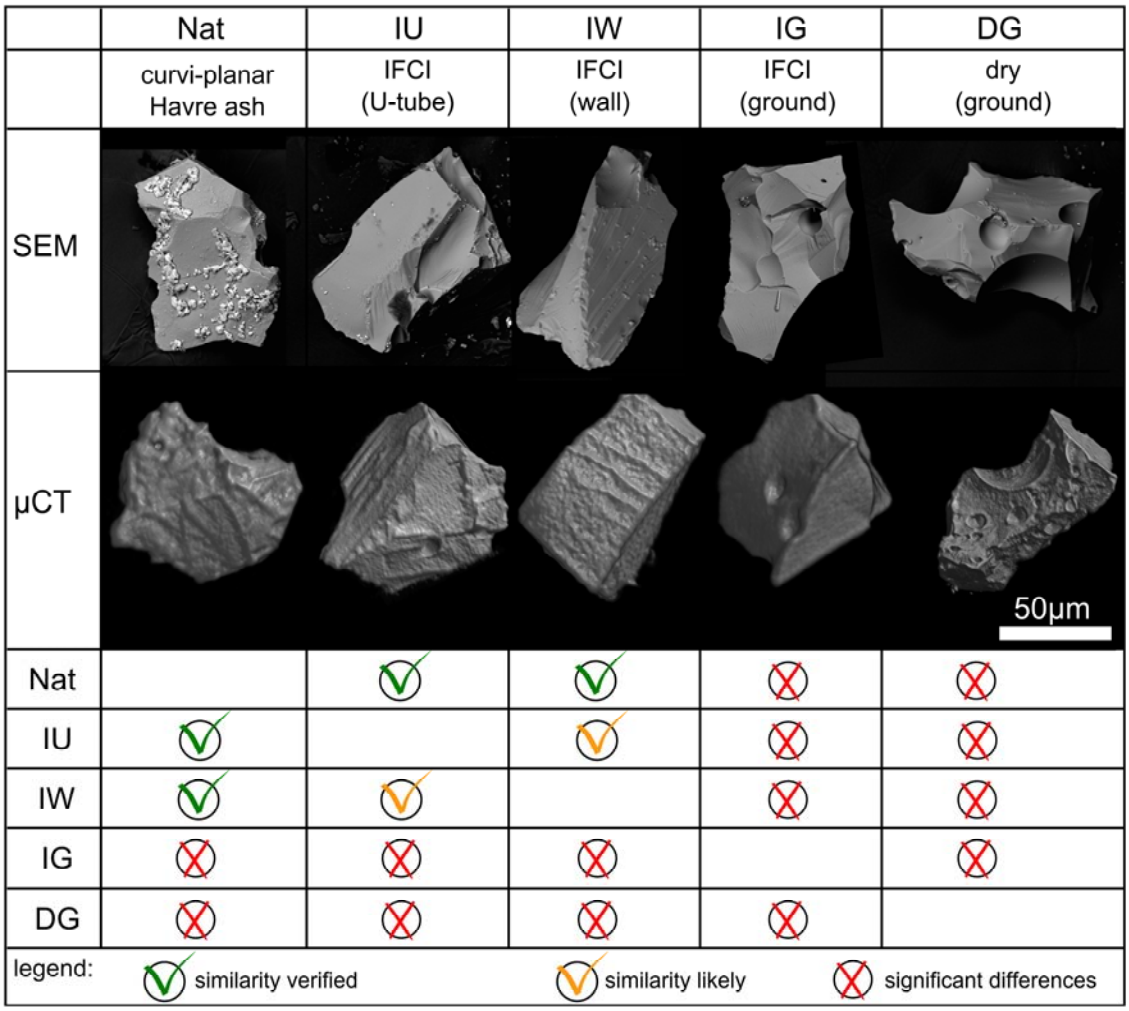

589

590 **Figure 4| Morphometric analysis results by t-tests and e-tests.** Typical particles imaged with SEM
591 and X-ray microtomography (image pixel size 0.56 µm). Natural ash ("Nat") is significantly similar to
592 particles from the leading ejecta front of IFCI experiments (IU and IW), which are highly similar to
593 one another.

594

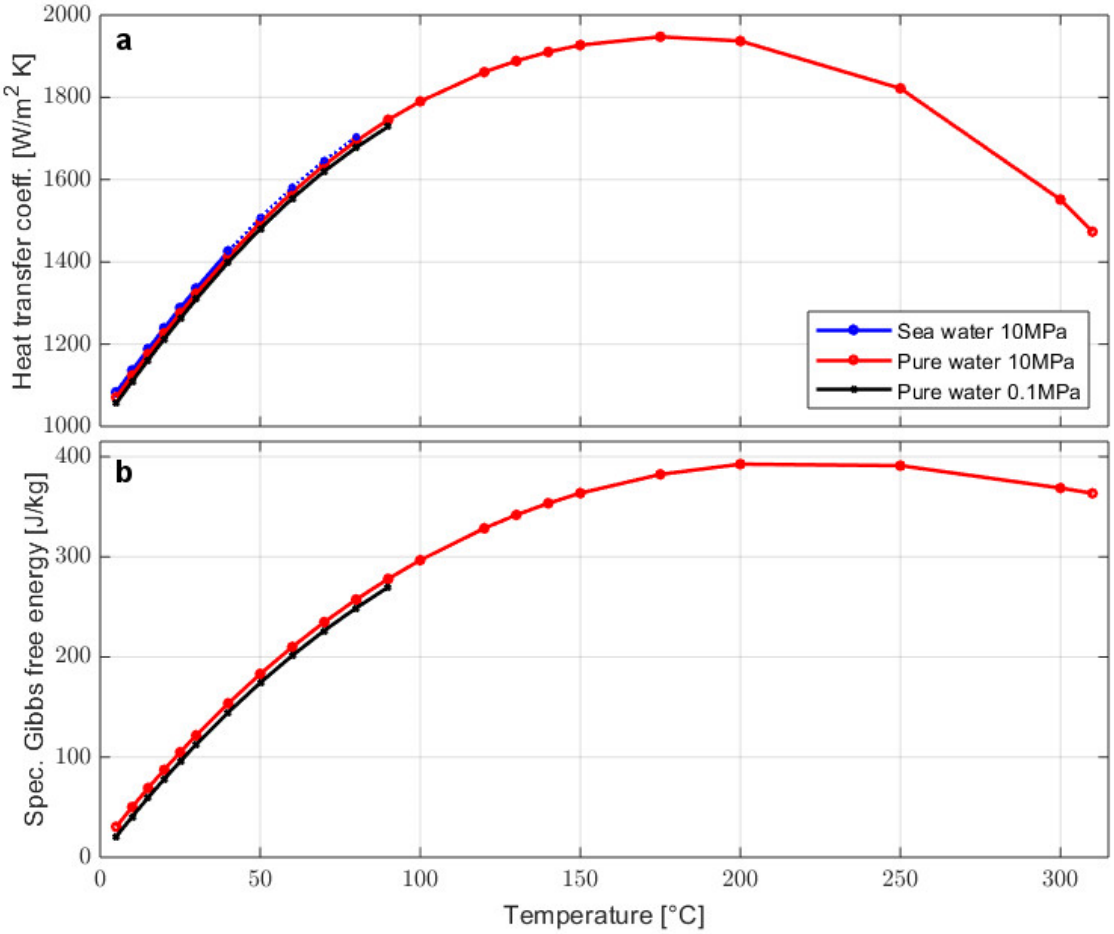

Figure 5| IFCI-relevant thermal water properties at lab and seafloor pressures. a, heat transfer coefficient *h* computed for water at atmospheric pressure (0.1 MPa; black) and 10 MPa (red), and for saline water from empirical laws tested for oceanic temperatures[45,47] (solid blue lines, see Methods). Dashed blue lines extrapolate results to 80°C. Water boils much hotter on the seafloor, allowing higher heat transfer coefficient values that increase IFCI efficiency under deep-sea conditions. **b**, This is also suggested by the curve for specific Gibbs free energy *G*. Dependencies of input parameters used to compute the heat-transfer coefficient are presented in Extended Data Fig. 4.